

Formation process of large ion Coulomb crystals in linear Paul traps

L. Hornekær* and M. Drewsen

Institute of Physics and Astronomy, Aarhus University, DK-8000 Aarhus, Denmark

(Received 4 January 2002; published 29 July 2002)

We report on the results on various aspects of the formation of ion Coulomb crystals in linear Paul traps, for plasmas containing from a few hundred to several thousand laser-cooled $^{24}\text{Mg}^+$ ions. The presented studies include observations of changes in emitted fluorescence, changes in plasma aspect ratio, and the formation of shell structure, during the transition from the cloudlike to the crystalline state. The competition between rf heating and laser cooling is observed to result in a very dramatic transition from the cloudlike disordered state to a liquidlike state. After the liquid state is reached ordering into shell structure takes place as a continuous process at even higher plasma coupling parameters. This is in contrast to earlier observations of few-ion plasmas in hyperbolic rf traps.

DOI: 10.1103/PhysRevA.66.013412

PACS number(s): 32.80.Pj, 42.50.Vk

I. INTRODUCTION

Ion Coulomb crystals [1,2], a unique ordered state of matter, are formed by cooling an ion plasma, with a density of the order of 10^7 – 10^8 cm^{-3} , to temperatures in the millikelvin regime. Reaching such low temperatures became possible with the advent of laser cooling [3]. Even though only a limited number of ion species can easily be laser cooled, the effect of sympathetic cooling [4,5] makes it possible to form multispecies ion crystals consisting of a wide range of atomic ions and even molecular ions [6,7]. Such single-species and multispecies crystals are a promising medium for performing a wide range of experiments in various fields of physics. It has been proposed to implement a quantum computer using a few ions in a string crystal [8], while larger ion crystals might be a future storage medium for quantum states of light and hence for quantum information encoded in light fields [7,9]. The cold, well localized ions in ion crystals can also serve as targets for spectroscopy experiments and might even constitute a future frequency standard [10]. In the field of accelerator physics, crystalline ion beams, offering the possibility to obtain unprecedented brilliance, have long been an elusive goal. Recently, however, the observation of a crystalline ion beam in radio frequency quadrupole storage ring was reported [11]. Apart from the possible applications, ion crystals have proven to be interesting objects in themselves, being an example of a finite, strongly coupled one-component plasma. While the infinite one-component plasma shows relatively well defined phase transitions between the gas, liquid, and solid states (a bcc structure), the finite plasmas show a more complex behavior. Though a spatially ordered state is reached at low temperatures, this state does not display real long-range order, but rather ordered structures defined by boundary conditions set by the trapping potentials. These structures range from one-dimensional (1D) ion strings, over 2D planar crystals, to 3D spheroidal crystals where the ions arrange themselves in concentric shells [1,2,12–16]. However, real 3D long-range or-

der in the form of a bcc structure has been observed at the center of very large spherical ion crystals containing above 10^5 ions [17] contained in a Penning trap. Also in Penning traps, a variety of structures exhibiting 2D long-range order has been observed in large planar and very oblate crystals [16,17]. In radio frequency Paul traps the attainable crystal sizes seem to be limited by the effect of rf heating [18].

For large finite plasmas, simulations do not predict an abrupt phase transition to the shell-structure state [19–21]. Experimental observations and simulations do, however, seem to indicate an abrupt transition to the ordered state for few-ion plasmas confined in hyperbolic Paul traps [1,18], sometimes described as a chaos-order transition [18,22–25]. The question of transitions between the disordered gaslike or cloudlike state and the spatially ordered state of such large finite ion crystals confined in radio frequency Paul traps is the topic of this paper. We present results on the transition from the cloud state to the ordered state, for ion plasmas containing a few hundred to several thousand ions. The significance of characteristic features of the fluorescence spectrum of a laser-cooled ion plasma, during the transition to the ordered state, is discussed and the emergence of shell structure and the change in aspect ratio, as function of the coupling parameter, are examined.

II. STRONGLY COUPLED ONE-COMPONENT ION PLASMAS

The thermodynamic state of a one-component ion plasma is governed by the plasma-coupling parameter Γ , defined as

$$\Gamma = \frac{Q^2}{4\pi\epsilon_0 a_{WS} k_B T}, \quad (1)$$

where Q is the charge of the ions, T is the plasma temperature, and a_{WS} is the Wigner-Seitz radius given by $a_{WS} = (4/3\pi n_0)^{-1/3}$, where n_0 is the zero-temperature particle density. Computer simulations show that the infinite plasma enters a liquidlike state for $\Gamma \approx 2$ [26], and an ordered crystalline state for $\Gamma \approx 170$ [27,28]. The transition from a cloudlike through a liquid to a solid state in finite ion plasmas, has

*Present adress: Institute of Physics, SDU, Odense University, DK-5230 Odense, Denmark.

been studied via molecular-dynamics (MD) simulations of ion plasmas confined in 3D harmonic potentials. These predict that the ions first separate in concentric spheroidal shells and then, at even higher Γ , order within the shells [19]. In MD simulations of spherical ion clouds containing a few hundred ions, periodic oscillations of the ion density, as function of the distance from the trap center, were already observed for $\Gamma \approx 2$ [19]. These oscillations were seen to have maximum amplitude at the edge of the plasma. As Γ was increased the amplitude of the oscillations increased, until for $\Gamma \approx 140$ the density between shells was seen to go to zero. Within each shell, however, diffusion persisted until $\Gamma \approx 300$ –400. Hence for $140 \leq \Gamma \leq 300$ the plasma could be described as a solid in the direction perpendicular to the shells, but as a liquid on the shells. For $\Gamma \gtrsim 300$ –400, a near 2D hexagonal lattice structure, adapted to the shell curvature, was observed on the shells. Similar qualitative predictions for the formation process have been made from MD simulations of spherical crystals in radio frequency Paul traps, i.e., including the full time dependence of the rf field [21], and for infinitely long, radially harmonically confined ion plasmas of cylindrical symmetry [29].

Previous experimental studies by other groups of the progression of order in large ion plasmas with increasing coupling parameter have been limited to a single Penning trap experiment, where the state of crystallization at two different coupling parameters, $\Gamma = 50_{-20}^{+30}$ and $\Gamma = 180_{-70}^{+90}$ was investigated [15]. However, in this experiment the different plasma-coupling parameters were obtained through different cooling schemes, and in two crystals with the same ion number but different shape. Our group has previously reported observations of shell structure formation in large plasmas [13]. These results are in agreement with the more elaborate studies presented in this paper.

III. EXPERIMENTAL SETUP

The ions are confined in a linear Paul trap [30] consisting of four parallel cylindrical electrodes in a quadrupole configuration. Each electrode is partitioned into three segments. By applying a dc voltage U_{dc} to the eight end segments and an rf voltage U_{rf} to diagonally opposite electrodes, an effective 3D harmonic confinement with cylindrical symmetry is achieved. The axial potential is well described by

$$\Phi_z(z) = \frac{1}{2} M \omega_z^2 z^2, \quad \omega_z^2 = 2 \kappa Q U_{dc} / M, \quad (2)$$

where M and Q are the mass and charge of the ions and κ is a constant related to the trap geometry. For $q = 2(QU_{rf}/Mr_0^2\Omega^2) \ll 1$ the effective radial potential is given approximately by

$$\Phi_r(r) = \frac{1}{2} M (\omega_r^2) r^2, \quad \omega_r^2 = \omega_\rho^2 - \frac{1}{2} \omega_z^2, \quad \omega_\rho^2 = \frac{Q^2 U_{rf}^2}{2M^2 r_0^4 \Omega^2}, \quad (3)$$

where U_{rf} and Ω are the amplitude and the frequency of the applied rf field and $r_0 = 1.75$ mm is the distance from the

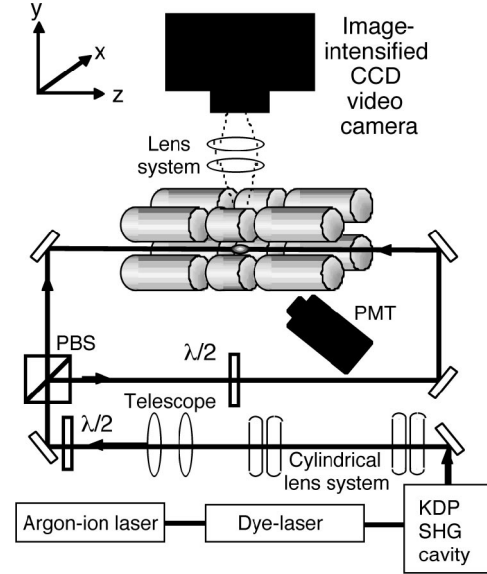


FIG. 1. Schematic overview of the experimental setup.

trap center to the surface of the electrodes. Two different traps were used for the experiments presented in this paper, differing only by the length of the center electrodes. The trap used for the fluorescence observations in Sec. IV had 25-mm-long center electrodes, which gave rise to a very weak axial potential, where only very prolate ion crystals could be formed. The second trap, used for the remaining experiments presented, had 4-mm-long center electrodes, making it possible to create prolate, spherical, and oblate ion crystals. Both traps were normally run at effective radial trapping frequencies of a few hundred kHz. The traps were placed in a UHV chamber with a typical background pressure of 2×10^{-10} Torr. The $^{24}\text{Mg}^+$ ions were loaded into the traps from thermal beams of neutral atoms. Ionization was achieved by electron impact, using a 1-keV electron beam. The $^{24}\text{Mg}^+$ ions were laser cooled on the $3s^2S_{1/2} \leftrightarrow 3p^2P_{3/2}$ transition, which has a natural linewidth $\Gamma_N = 45$ MHz and is resonant with light at 280 nm. Light at this wavelength was produced by frequency doubling the 560-nm output beam from an Ar-ion laser pumped dye laser using a potassium dihydrogen phosphate crystal in an external frequency doubling cavity. Laser cooling was done along the trap axis, using two counterpropagating laser beams of equal intensity, obtained by splitting the 280-nm output beam from the external frequency doubling cavity. The light, spontaneously emitted by the ions during the laser-cooling cycle, was monitored by a photomultiplier tube or imaged onto an image intensified digital charge-coupled device (CCD) video camera by a 15x magnification lens system, giving a spatial resolution of approximately $1 \mu\text{m}$. Laser frequency scan rates were varied between experiments ranging from 80 MHz/s to 1.33 GHz/s, depending on the monitoring system used. In Fig. 1 an overview of the experimental setup is shown.

IV. FLUORESCENCE OBSERVATIONS

One of the well-known signs of emerging order in few-ion plasmas in Paul traps has, from the first experiments, been

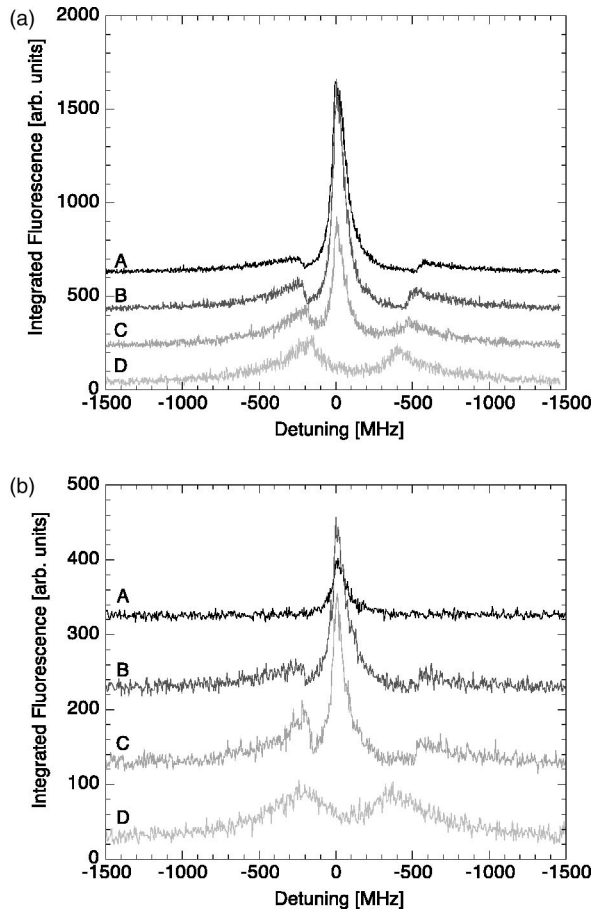


FIG. 2. (a) Fluorescence spectra at different powers of the cooling laser. Curve A: P_{max} , curve B: $0.57P_{max}$, curve C: $0.43P_{max}$, and curve D: $0.37P_{max}$. The background level has been offset by 200 counts between the different curves. (b) Fluorescence spectra at different rf amplitudes. Curve A: $U_{rf} = 30$ V, curve B: $U_{rf} = 40$ V, curve C: $U_{rf} = 50$ V, and curve D: $U_{rf} = 60$ V. The background level has been offset by 100 counts between the different curves.

the appearance of a sudden drop in fluorescence level [1], here referred to as the *fluorescence dip*. The fluorescence dip can be observed by variation of the laser-cooling force or rf amplitude [1]. In this paper, the fluorescence level as a function of the laser-cooling force is studied by changing the laser frequency. The fluorescence intensity was monitored by a photomultiplier tube. Figure 2(a) shows the fluorescence as a function of laser detuning for different laser powers. The background level has been offset by 200 counts between the different curves. The detuning is first scanned towards resonance. Just before reaching resonance, close to the optimum detuning for laser cooling, $\Gamma_N/2$, the scan is stopped, and the laser is scanned back towards an initial detuning of -4 GHz. All detunings, δ , given in this paper are with respect to the optimum detuning $\sim \Gamma_N/2$. The frequency scan rate employed in the experiments described below was 1.33 GHz/s $\sim 30\Gamma_N/s$ [31]. On all curves, except for the low-power curve (curve D), a peak is seen at a detuning $\delta \sim 0$ MHz. This is the fluorescence signal from the cold ion plasma, which at the minimum detuning was identified on

CCD camera images as being in the crystalline state. In the region $\delta \sim -300$ to -150 MHz on the up-scan, and $\delta \sim -450$ to -600 MHz on the down-scan, the fluorescence dips are seen. These spectra show several interesting features. First, a hysteresis effect is seen. The dip in fluorescence occurs for a smaller detuning in the up scan than in the down-scan. Assuming that the dip marks a transition to a more ordered state, this indicates that a larger laser-cooling force is needed to make the transition into this state, than to keep the ions in the state, once it is established. A similar result was obtained for up to five-ion plasmas in a hyperbolic Paul trap [1]. A second feature is the dependence upon laser power. As the laser power is lowered the dip occurs at smaller and smaller detunings as expected, since at lower laser power a smaller detuning is needed to have equally high cooling rates, but at the lowest laser power, curve D, the ion plasma never enters into the crystalline state. There is no intensity peak at zero detuning. Still something resembling the dip is seen, at a detuning that seems to lie in natural continuation of the dips seen for higher laser powers. In Fig. 2(b) the fluorescence intensity as function of rf amplitude U_{rf} is shown. The background level has been offset by 100 counts between the different curves. At $U_{rf} = 30$ V, curve A, no fluorescence dip is discernible above the background noise, but still we have a fluorescence peak at zero detuning, and could, on CCD camera images, identify the plasma as being in the crystalline state close to resonance. At $U_{rf} = 60$ V, curve D, a situation equivalent to the low laser power scan is seen: No crystallization, but still the rise in fluorescence normally indicating the beginning of the fluorescence dip.

The fluorescence dip can be seen as a result of a competition between the rf-heating effect and the laser-cooling force [25]. This is supported by Fig. 2(b), showing that the rf amplitude has a strong effect on the size of the intensity change at the fluorescence dip, and that for sufficiently high rf amplitude, no crystallization occurs. Also, in Penning traps, where no rf heating is present, no fluorescence dip is observed [32]. It has been argued that the fluorescence dip, a result of a sudden narrowing of the ion velocity distribution leading to a reduction of the number of ions in resonance with the frequency detuned laser, is an indication of the transition between cloud and crystalline states [1]. For small ion plasmas containing five or less ions, confined in a hyperbolic Paul trap, observations have confirmed that, starting in a cloud state, an ordered structure is present after the dip [1] and vice versa. Whether this result can be generalized to larger ion plasmas is one of the main questions raised in this paper. Based on the observations presented above we conclude that the observation of a fluorescence dip is not a necessary condition for reaching the crystalline state, see curve A in Fig. 2(b). Whether observation of a fluorescence dip is a sufficient condition for identifying a transition into a crystalline state is discussed in the following sections.

V. ASPECT RATIO OF STRONGLY COUPLED PLASMAS DURING FORMATION

The outer shape of an ion crystal has been found to be well described by a zero-temperature charged liquid model

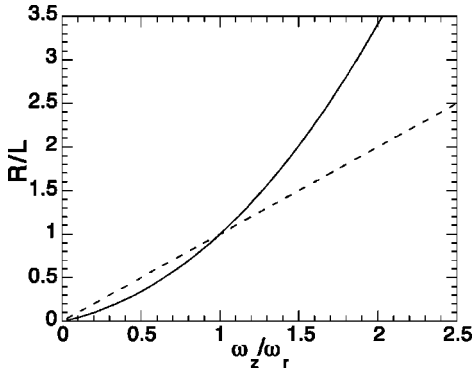


FIG. 3. The relation between the ratio of the axial and radial oscillation frequencies and the crystal aspect ratio for a zero-temperature charged liquid, solid line, and for weakly coupled particles in thermodynamic equilibrium, dashed line.

[7]. For a zero-temperature charged liquid confined in a cylindrically symmetric 3D harmonic potential, the equilibrium shape is a constant density spheroid [33]. The aspect ratio of the spheroid, defined as the ratio between the spheroid half-length L and radius R , $\alpha = R/L$, depends on the ratio between the axial, ω_z , and radial, ω_r , oscillation frequencies of the trapping potential. Based on the calculations in Ref. [33] the following relations can be shown to be valid.

In the oblate case, $\alpha = R/L > 1$,

$$\frac{\omega_z^2}{\omega_r^2} = -2 \frac{\sin^{-1}(1 - \alpha^{-2})^{1/2} - \alpha(1 - \alpha^{-2})^{1/2}}{\sin^{-1}(1 - \alpha^{-2})^{1/2} - \alpha^{-1}(1 - \alpha^{-2})^{1/2}}, \quad (4)$$

and in the prolate case, $\alpha = R/L < 1$,

$$\frac{\omega_z^2}{\omega_r^2} = -2 \frac{\sinh^{-1}(\alpha^{-2} - 1)^{1/2} - \alpha(\alpha^{-2} - 1)^{1/2}}{\sinh^{-1}(\alpha^{-2} - 1)^{1/2} - \alpha^{-1}(\alpha^{-2} - 1)^{1/2}}. \quad (5)$$

The relation between the ratio of the trapping frequencies and the plasma aspect ratio, as found above, has previously been shown to be valid for liquidlike ion plasmas in Penning traps [34] and, for not too extreme aspect ratios, for single and multispecies ion crystals in radio frequency Paul traps [7]. Equations (4) and (5), are shown in Fig. 3, together with the relation for weakly coupled particles in thermodynamic equilibrium, $\alpha = \omega_z/\omega_r$. As can be seen, the aspect ratio, for a given value of ω_z/ω_r , can be quite different for the weakly coupled case, i.e., particles in a hot cloud, and the strongly coupled case, i.e., particles in the liquid to crystalline phase. Also the density distribution of the ion plasma changes from being a Gaussian distribution at high temperatures to being a uniform distribution in the liquid low-temperature state, with emerging shell structure at even lower temperatures. In this section and the following section, experiments, aimed at investigating how the aspect ratios change as the coupling parameter is increased, especially near the fluorescence dip, and investigating whether or not shell structure is present right after the fluorescence dip, are presented.

The shell-structure formation and aspect ratio change were investigated for four different crystals, a small and a large prolate crystal and a small and a large oblate crystal.

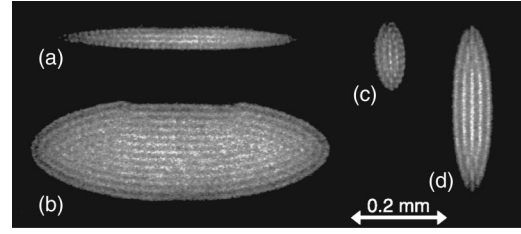


FIG. 4. CCD images of (a) small prolate crystal containing approximately 200 $^{24}\text{Mg}^+$ ions, (b) large prolate crystal containing approximately 2800 $^{24}\text{Mg}^+$ ions, (c) small oblate crystal containing approximately 175 $^{24}\text{Mg}^+$ ions, (d) large oblate crystal containing approximately 1100 $^{24}\text{Mg}^+$ ions.

Pictures of the four crystals are shown in Fig. 4. The image intensified digital CCD camera was used for monitoring both the total fluorescence and the spatial distribution of the ions. The measurements were performed by scanning the laser from a detuning of -2 GHz towards resonance and back again. The frequency scan was performed at a scan rate of 125 MHz/s for the small crystals and 80 MHz/s for the large crystals. At frame rates of 5 frames/s this gives a frequency resolution of the images of 25 MHz/frame ($\sim \Gamma/2$) for the small crystals and 16 MHz/frame ($\sim \Gamma/3$) for the large crystals. The total fluorescence from the ions was obtained from the images by integrating the fluorescence counts over all pixels.

Figure 5 shows the fluorescence spectra and the aspect ratios for the different crystals, as a function of the laser detuning. Due to the variation in density distributions for different coupling parameters, three different measures of the aspect ratios are given. The direct measure of the aspect ratio is obtained by measuring the minor and major axes in the ellipsoid formed by the projection of the outer shell onto the image plane, for the crystal image recorded at the smallest laser detuning. In practice, this was done by extracting the details in the image by subtracting the relatively slowly varying fluorescence contributions from ions performing micro-motion in the image plane [35]. The axial and radial positions of the outer shell were then found by making a projection of a slice through the center of the crystal, in the detail enhanced version of the image, onto the axial or radial plane, respectively, and subsequently doing a Gaussian fit to the intensity distribution in the outer shell. After having measured the major and minor axes using this technique, the actual direct measure of the aspect ratio was calculated using the expression

$$\alpha = \frac{R_{meas} + 1.48a_{ws}/2}{Z_{meas} + 1.48a_{ws}/2}, \quad (6)$$

where $1.48a_{ws}/2$, approximately equal to half the intershell spacing [20], is added to emulate a constant density distribution. This measurement method has previously been used to demonstrate that Eqs. (4) and (5) correctly describe the shape of single-species and multispecies ion crystals in radio frequency Paul traps [7]. It is of course only applicable for ion plasmas in the shell structure phase. The aspect ratio com-

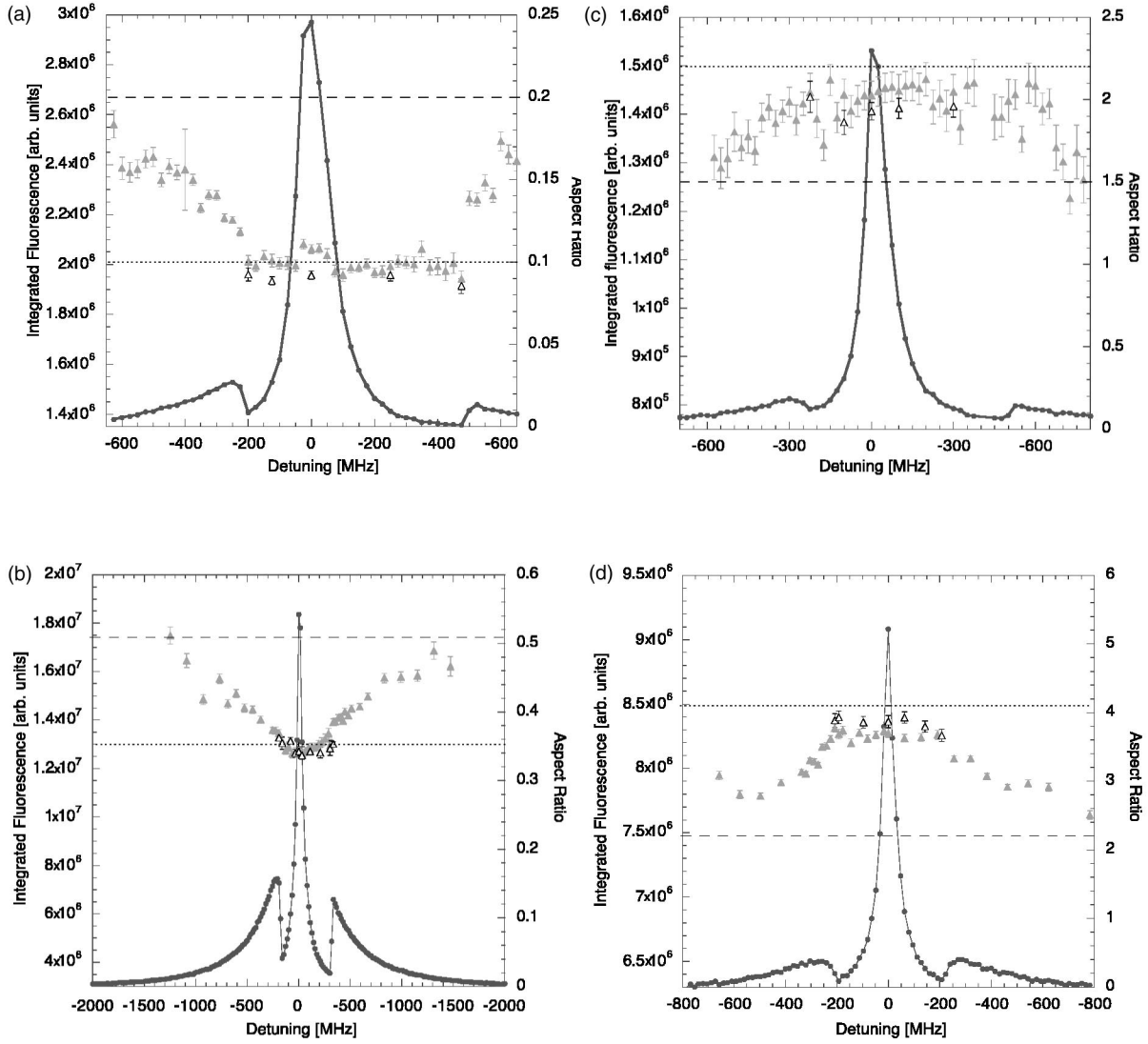


FIG. 5. Fluorescence level \bullet (the curve is a guide to the eye) and aspect ratio R/L for (a) the small prolate crystal shown in Fig. 4(a), (b) the large prolate crystal shown in Fig. 4(b), (c) the small oblate crystal shown in Figs. 4(c), and (d) the large oblate crystal shown in Fig. 4(d). In all graphs aspect ratios derived from Gaussian fits are marked by gray \blacktriangle and constant density spheroid fits are marked by \triangle . The dotted line marks the aspect ratio determined from the direct measure, i.e., equivalent to the zero-temperature charged liquid model prediction, while the dashed line marks the corresponding aspect ratio for weakly coupled particles. The error bars indicate the uncertainties from the fits.

puted using this method was used to calibrate the value of ω_z/ω_r , in all cases giving values well within the uncertainty of the measured ω_z/ω_r .

The aspect ratio was also measured by making a Gaussian fit to the intensity distribution of a projection of a radial or axial cross section through the center of the original image. The aspect ratio was then computed as $\alpha = \sigma_r/\sigma_z$, where σ_r and σ_z are the Gaussian widths obtained from the fits to the radial and axial cross sections. These measurements are referred to as Gaussian fits in Fig. 5 and are the best estimate for aspect ratios when the ion plasma is in the gas phase. However, in the liquid and shell-structure phase the Gaussian fits are not very good estimates.

Finally, the aspect ratio was calculated by fitting the measured intensity distributions in the cross-section projections to the intensity distribution obtained from a cross section

through a constant density spheroid. The linear density distribution of a cross section through the center of a constant density spheroid is given by

$$\lambda_{cd,\xi} = \lambda_0 \sqrt{1 - \frac{(\xi_0 - \xi)^2}{\xi_{edge}^2}}, \quad (7)$$

where λ_0 is the maximum intensity, ξ denotes either the radial, r , or axial, z , coordinate, ξ_0 denotes the radial, r_0 , or axial, z_0 , crystal center, and ξ_{edge} denotes the position where the intensity is equal to the background level, i.e., the plasma half-width, where r_{edge} is the plasma half-width obtained from a fit to the radial projection and z_{edge} is the plasma half-width obtained from the fit to the axial projection. The aspect ratio was then computed as $\alpha = r_{edge}/z_{edge}$. The con-

stant density spheroid distribution was generally seen to be a very good estimate close to the dip. However, the fit to distributions with pronounced shell structure in some cases gave an overestimate of the crystal width, see later discussion.

In Fig. 5(a) the aspect ratio for the small very prolate crystal containing approximately 200 ions [see Fig. 4(a)] is shown. On the laser frequency up-scan, the aspect ratio is seen to decrease with decreasing detuning and to reach a constant level, equivalent to the aspect ratio given by the direct measure and to the predictions of the zero-temperature charged liquid model, at the point of the fluorescence dip at $\delta \approx -200$ MHz. On the down-scan, a discontinuous jump to a higher aspect ratio is observed in connection with the fluorescence rise at $\delta \approx -500$ MHz, while on the up-scan only a small jump in aspect ratio is seen.

An almost similar behavior is seen in Fig. 5(b), where the fluorescence level and aspect ratio for the large, 2800-ion, prolate crystal are shown. However, here a jump in aspect ratio at the dip is only visible on the down-scan, while a more continuous transition is observed on the up-scan. Due to the large number of ions, it was possible to make fits to the intensity distributions even at large detunings, where the aspect ratio for uncoupled particles is approached. From the image of the large prolate crystal shown in Fig. 4(b) it is clear that the crystal contains some impurity ions, situated in the outer shell of the crystal [36]. Due to the presence of dark ions, only the lower half (in the image) of the crystal was used for obtaining the Gaussian and constant density spheroid fit. The center was found from the Gaussian fits of the plasma in the gas state, where the different species are supposed to mix.

In Figs. 5(c) and 5(d) fluorescence level and aspect ratios for a small, 175-ion, and a large, 1100-ion, oblate crystal [see Figs. 4(c) and 4(d)] are shown. The aspect ratios derived from the fits deviate somewhat from the directly measured and predicted aspect ratios, however, an increase in the fluorescence level up to the fluorescence dip on up-scan is observed and in both cases a relatively constant level is reached at small detunings.

In general, the aspect ratios obtained from the constant density spheroid and the Gaussian fits agree rather well, however, the agreement between the fits and the direct measurement is most convincing in the case of the prolate crystals. The deviations in the case of the oblate crystals are attributed to the fact that both types of fits were not particularly good in the case of pronounced shell structure. In the oblate crystals this effect is worse, since the density along the axis almost goes to zero between crystal planes, see Fig. 6. Such large density modulations, with sharp peaks right at the edge of the crystal, cause an overestimate of the crystal widths in the fits. Even right after the dip, where shell structure is not yet established (see later), an overestimate in the axial plasma width is seen due to large density fluctuations in the ion plasma; see, e.g., Fig. 6.

The effect of the sharp outer peaks is also seen in the radial and axial second intensity moments of the crystals, calculated directly from the background subtracted images, as

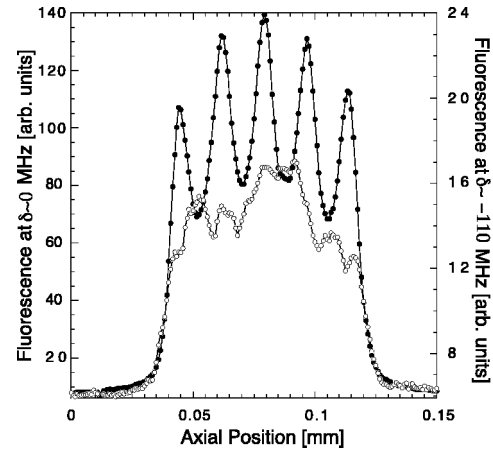


FIG. 6. A projection of an axial cross section through the center of the large oblate crystal is shown at two different detunings, ● marks the fluorescence at $\delta \sim 0$ MHz, with respect to the optimum detuning for laser cooling, pronounced shell, or planar, structure is clearly visible. ○ marks the fluorescence at $\delta \sim -110$ MHz, where the ion plasma is in the liquid state. The outer edge of the plasma is seen to coincide in the two cases.

$$M_x = \frac{\sum_{\text{all pixels } (x,z)} (x-x_0)^2 I_{x,z}}{\sum_{\text{all pixels } (x,z)} I_{x,z}}, \quad (8)$$

where x_0 is the weighted center along the x axis, see Fig. 1, and $I_{x,z}$ is the intensity in the point with coordinates (x,z) . M_z is calculated according to a similar formula. In Figs. 7 and 8 the second intensity moments in the radial direction,

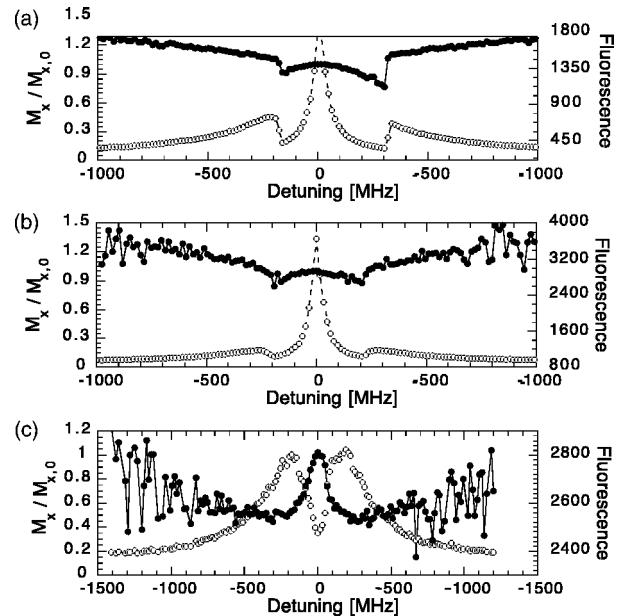


FIG. 7. Radial second intensity moments, normalized to the value at resonance ●. Integrated fluorescence ○. (a) The large prolate crystal, (b) the large oblate crystal, and (c) a scan towards resonance at a laser power too low for crystallization.

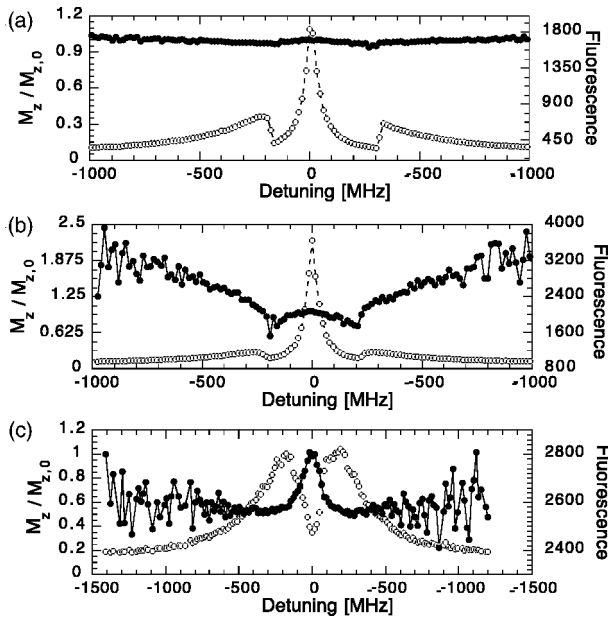


FIG. 8. Axial second intensity moments, normalized to the value at resonance ●. Integrated fluorescence ○. (a) The large prolate crystal, (b) the large oblate crystal, and (c) a scan towards resonance at a laser power too low for crystallization.

M_x , and in the axial direction, M_z , respectively, are shown for the two large crystals, Figs. 4(b) and 4(d), at various detunings. For comparison, a scan towards resonance at a laser power too low for crystallization is also shown. The second intensity moments are normalized to the value at resonance. In both cases where a crystal is formed, the fluorescence dip is associated with a volume contraction, resulting from a contraction in one or both of the radial and axial directions. After this contraction an increase in the second intensity moments is observed. This is due to the fact that a shell-structure distribution, with a sharp outer peak at the crystal edge, will have a larger second moment than a constant density spheroid distribution. Hence the increase in second intensity moments is not an effect of an increased radial or axial position of the outer edge of the plasma. In Fig. 6 this is clearly shown. Here the projection of an axial cross section through the center of the large oblate plasma is shown at two different detunings. The outer edges of the ordered and the liquid plasmas are seen to coincide, even though the second moments differ for the two cases. In the case where the laser power is too low to crystallize the ion plasma, an increase in volume along with a drop in fluorescence is observed at small detunings. In this last case, the rf heating overcomes the effect of the laser-cooling, leading to a rapid heating of the ion cloud, resulting in large ion displacements and velocities, bringing the ions out of resonance with the cooling laser.

To summarize, changes in aspect ratio as function of plasma coupling parameter were studied by varying the laser-cooling force via the laser detuning. In the case of prolate ion plasmas, an increase in the coupling parameter leads to a decrease in aspect ratio. In the cloud state, the aspect ratio was seen to decrease continuously, while at the fluorescence dip a more or less pronounced discontinuous change to

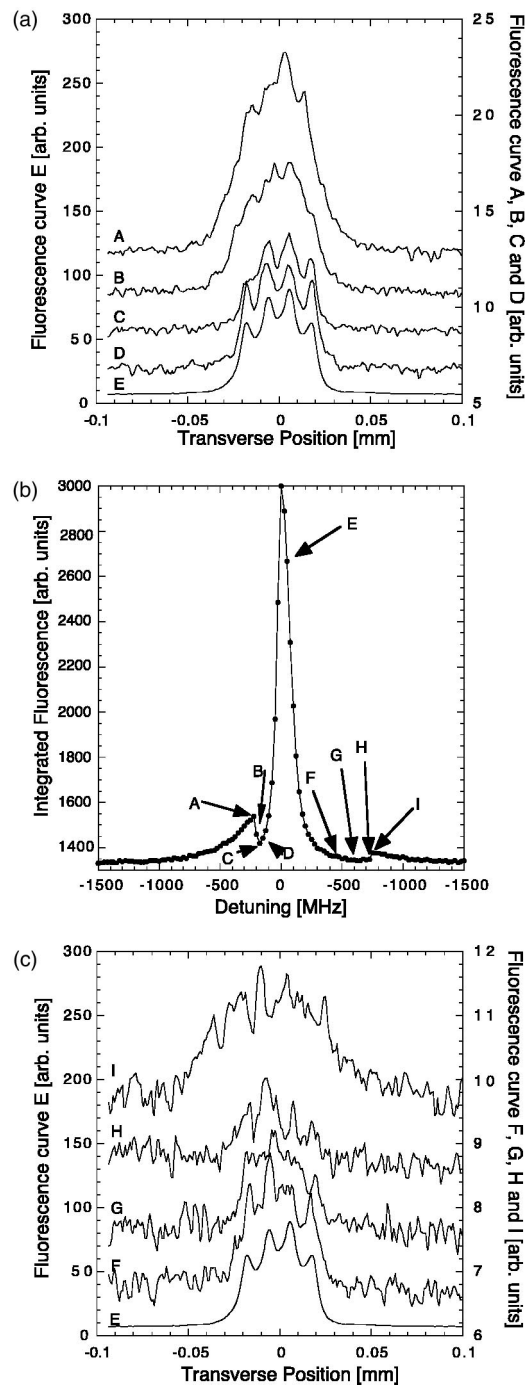


FIG. 9. Shell-structure formation in the small prolate crystal shown in Fig. 4(a). a. Projections onto the x-axis of cross-sections through the center of the ion plasma are shown at 4 different detunings, A-D, indicated in Fig. 9(b), during the scan towards resonance. The background-level has been offset by 200 counts between the different curves. Curve E, shown on a different scale, displays the cross-section in the fully crystallized state. b. The integrated fluorescence level during the frequency scan towards resonance, and back again. c. Projections onto the x-axis of cross-sections through the center of the ion plasma are shown at 4 different detunings, F-I, indicated in Fig. 9(b), during the scan away from resonance. The background-level has been offset by 100 counts between the different curves. Again curve E, the cross-section in the fully crystallized state, is shown on a different scale.

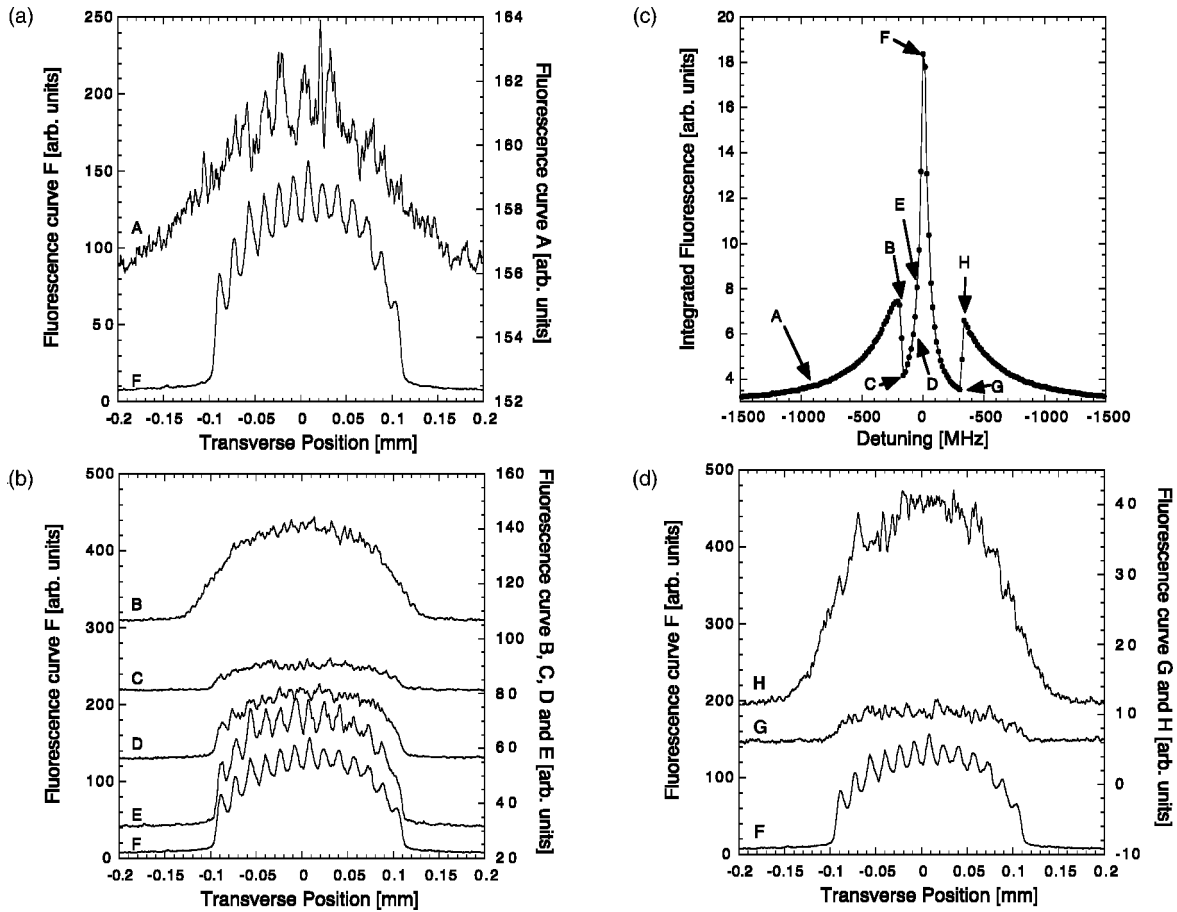


FIG. 10. Shell-structure formation in the large prolate crystal shown in Fig. 4(b). (a) Projections onto the x axis of cross sections through the center of the ion plasma are shown at two different detunings, far from resonance, curve A, and at resonance, curve F, indicated in Fig. 10(c). (b) Projections onto the x axis of cross sections through the center of the ion plasma are shown at four different detunings, B–E, indicated in Fig. 10(c), during the scan towards resonance. The background level has been offset by 25 counts between the different curves. Curve F, shown on a different scale, displays the cross section in the fully crystallized state. (c) The integrated fluorescence level during the frequency scan towards resonance, and back again. (d) Projections onto the x axis of cross sections through the center of the ion plasma are shown at two different detunings, G and H, indicated in Fig. 10(c), during the scan away from resonance. The background level has been offset by three counts between the different curves. Again curve F, the cross section in the fully crystallized state, is shown on a different scale.

a lower value was observed. The minimum aspect ratio reached was seen to be in good agreement with the predictions of the zero-temperature charged liquid model. For oblate crystals an increase in aspect ratio towards an almost constant level, deviating somewhat from the predictions of the zero-temperature charged liquid model, was observed for increasing coupling parameter. Accurate and comparable measurements of the aspect ratio over a large range of detunings are made difficult by the fact that no single method was found, which could be used to measure the spatial extent of the ion plasma in the cloudlike, liquidlike, and shell-structure phases. Finally, the fluorescence dip was seen to be associated with a volume contraction. In the cases where the laser power was too low for crystallization, the reverse effect was seen, and an increase in volume was observed at small detunings along with a drop in fluorescence level. The drop in fluorescence, in the cases where the transition to the liquidlike state is not made, happens at a detuning that seems to lie in natural continuation of the detunings at which a tran-

sition into the liquidlike state is obtained, see Figs. 2(a) and 2(b). This indicates that at these detunings a critical state or density is reached, where either laser cooling wins and the ion cloud collapses into the liquidlike state, or rf heating wins leading to rapid heating of the ion cloud.

VI. SHELL-STRUCTURE FORMATION

Apart from the significant changes in aspect ratio, the formation of shell structure in the four cases discussed above was also studied. Figure 9 displays the spatial structure in the small 200-ion prolate crystal discussed above, at various detunings. The projections shown, are projections onto the x axis of radial cross sections through the center of the ion plasma. The images, and hence the projections, show fluorescence contributions both from ions situated close to the x - z -center plane, these perform micromotion in the y direction and cause the well defined shell structure visible in projections and images, and from ions situated out of the

x - z -center plane, performing micromotion in the x direction, giving rise to a blurred fluorescence background over the extent of the crystal. Hence, in the images and projections the fluorescence level between the shells would not go to zero even in the case of complete crystallization. For clarity the background level has been offset between the different curves (see figure caption). Pronounced shell structure is visible right after the dip, curve C , indicating that the drop in fluorescence and the transition into a crystalline state take place simultaneously. This is in agreement with previous observations of small ion plasmas in hyperbolic Paul traps, showing that right after the dip, the ions were spatially ordered. Just before the fluorescence dip, curve A , a density distribution with a broad Gaussian base and large density fluctuations in the center of the plasma are seen. On the down-scan, however, the shell structure appears to be gone before the fluorescence rise at $\delta \approx 750$ MHz, curve G , but the outer radius is still equivalent to the radius of the shell-structure state, and even in the image right before the fluorescence rise, curve H , a weak indication of peaks is seen at the positions of the shells. Curve I shows the cross section right after the dip, where the plasma has returned to the cloudlike state.

In Fig. 10 similar measurements on the large 2800-ion prolate crystal are shown. Curve A shows the cross section of the ion plasma in the cloudlike state, while curve F shows the fully crystallized ion plasma. For the large crystal shown here, the shell structure does not appear right after the dip, see curves C and D . A number of peaks are present, but these appear, as often as not, at positions where no shells are observed to be present in the crystalline state at smaller detuning, compare curves C and D with curves E and F . Real shell structure is observed at a detuning of $\delta \approx -50$ MHz from the optimum detuning, curve E , while the fluorescence dip occurs at a detuning of $\delta \approx -160$ MHz, curves B and C . Similarly on the down-scan, the shell structure disappears before the fluorescence rise, see curve G . These results are in good agreement with our previous studies of shell-structure formation in large crystals [13] and indicate that for large ion crystals a liquidlike state, as opposed to a crystalline state, is reached at the fluorescence dip.

Even though shell structure appears at a smaller detuning than the fluorescence dip, the measurements show that spatial separation of different mass ions, see Ref. [7], takes place right at the fluorescence dip. This is further indicating that at this point the liquidlike state is reached. The small number of impurity ions present in the crystal are seen to be located in the upper (in the image) outer shell. This gives rise to an asymmetry in the shell-structure profile in the crystalline state compared to the Gaussian profile in the cloudlike state, compare curves A and F in Fig. 10. The segregation between the different mass ions is identified by noticing that this asymmetry in the cross-section projections appears right after the dip, compare curves C and F . Right after the dip, curve C , the outer radius is seen to be similar to the radius of the plasma in the crystalline state, curve F .

In Figs. 11 and 12, projections onto the z axis of cross sections through the center of the small and the large oblate plasmas discussed above, are shown. In Fig. 11(a), a projec-

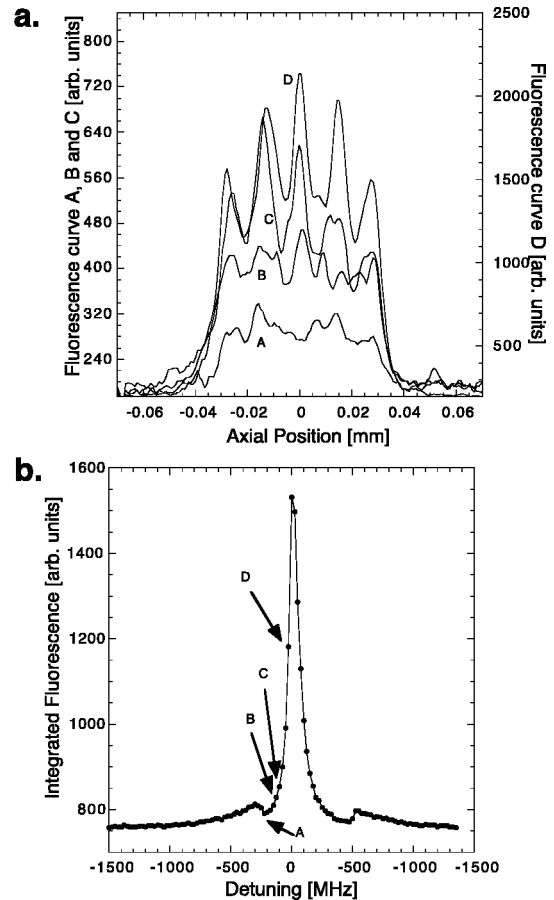


FIG. 11. Shell-structure formation in the small oblate crystal shown in Fig. 4(c). (a) Projections onto the x axis of cross sections through the center of the ion plasma are shown at four different detunings, A – D , indicated in Fig. 11(b), during the scan towards resonance. (b) The integrated fluorescence level during the frequency scan towards resonance, and back again.

tion of the cross section right after the dip, at $\delta = -225$ MHz, curve A , is shown. Some peaks in intensity are seen, but for example, the central peak is missing, indicating that complete shell-structure ordering is not yet reached. Even at a detuning of $\delta = -125$ MHz, curve B , the shell structure is still not completely defined. In Fig. 12 cross sections obtained at detunings below $\delta = -80$ MHz, well below the detuning of the fluorescence dip at $\delta = -190$ MHz, are shown. At $\delta = -80$ MHz, curve A , no pronounced shell structure is present, but some modulation of the fluorescence intensity is seen, especially, some peak structure is visible at the edges of the plasmas. At a detuning of $\delta = -65$ MHz, curve B , weak indications of peaks at all shell positions are visible. These become gradually more pronounced as the detuning is further decreased, see curves C – F .

In conclusion, even though shell-structure ordering is observed right after the dip in the case of the small 200-ion prolate crystal, this is not the case for the larger crystals, or for the small 175-ion oblate crystal. However, in all cases the fluorescence dip is associated with a contraction in both the radial and axial directions, and also with a spatial segregation of different mass ions.

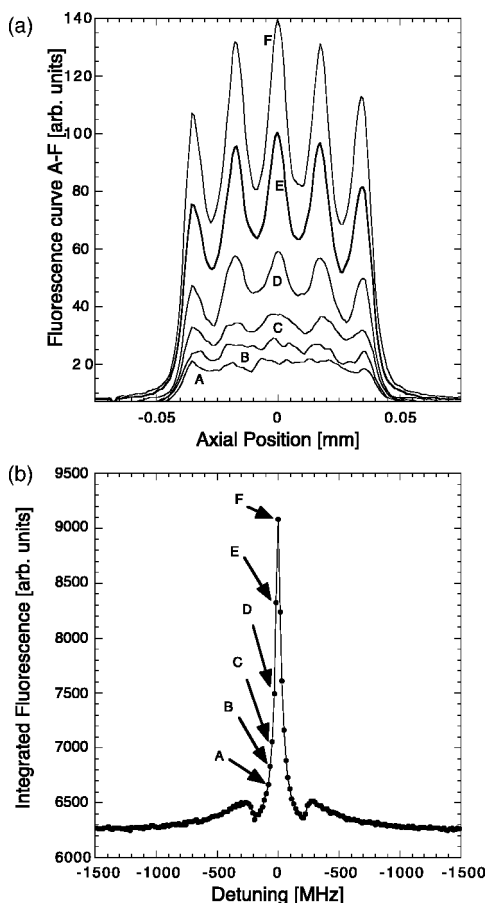


FIG. 12. Shell-structure formation in the large oblate crystal shown in Fig. 4(d). (a) Projections onto the x axis of cross sections through the center of the ion plasma are shown at six different detunings, A–F, indicated in Fig. 12(b), during the scan towards resonance. (b) The integrated fluorescence level during the frequency scan towards resonance, and back again.

In the case of very large ion crystals containing 10^4 – 10^5 ions, the fact that no shell-structure ordering is present after the dip becomes even more obvious, since in some of these cases it was not possible to reach the shell-structure phase at all.

It has previously been demonstrated by our group that it is possible to load ions directly into the liquidlike state and for small ion plasmas even directly into the crystalline state using the technique of resonance-enhanced two-photon ionization [37]. This method makes it possible to form huge liquidlike plasmas showing some degree of shell structure. Such a plasma is shown in Fig. 13. It contains approximately 40 000 $^{40}\text{Ca}^+$ ions, which in the crystalline state would be arranged in 22 shells. The plasma shown in Fig. 13 is, however, not completely crystallized. One or two outer shells are visible, but no further shell structure is seen. That this is not only a consequence of the huge extent of the ion plasma, causing the shell structure to be wiped out by the fluorescence of a huge number of ions moving in the image plane, was checked by sending a tightly focused probe laser into the center of the crystal, and chopping the cooling laser [38] in phase with a gate pulse for the image intensifier. The chop-

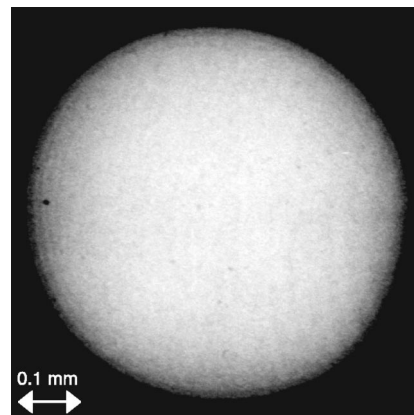


FIG. 13. Huge liquid $^{40}\text{Ca}^+$ plasma formed by resonance-enhanced two-photon ionization.

ping was done using an acousto-optic modulator at frequencies between 100 kHz and 1 MHz. The digital CCD video camera with a gateable image intensifier was used such that signal was only transmitted, when the cooling laser was off. However, no further shell structure was seen in the path of the tightly focused probe [39]. We therefore expect that the plasma-coupling parameter of such huge plasmas must be around $\Gamma \sim 20$, see Fig. 3 in Ref. [21], corresponding to a plasma in a liquidlike state at a temperature around 100 mK.

Earlier experiments show that starting from a plasma of similar size in the cloudlike state, it would not have been possible to reach the liquid phase. This is due to the fact that while the laser-cooling force saturates at some value specific for the ion-species cooled, the micromotion amplitude, and hence also the rf heating, keeps on growing with increasing crystal radius. Hence in this case the laser-cooling force would not be sufficient to overcome the large rf heating during the volume contraction prior to the transition from the cloudlike to the liquidlike state, and a transition to the liquidlike state with the associated dip in fluorescence would not occur. Instead rf heating would win, causing rapid heating of the cloud and spatial expansion, see Figs. 7(c) and 8(c). In the case of the liquid plasma shown in Fig. 13 the laser-cooling force is sufficient to keep the ions in the liquid state once it is created, but not sufficient to fully crystallize the ion plasma. Why these huge plasmas could not be cooled to temperatures sufficiently low for crystallization, is unknown. One theory is that the rf heating, due to the huge micromotion of the outer-shell ions, pumps enough energy into the system to maintain a steady state at relatively high temperatures, even in the presence of laser cooling.

Molecular-dynamics simulations of both small [40], and larger systems [21,41], show that for completely ordered systems, rf heating is negligible. In fact, the simulations of crystals containing 1000 ions, presented in Ref. [21] show that the rate at which kinetic energy is coupled from the rf motion into the secular motion, increases quadratically with temperature, and that for $\Gamma > 100$, rf-heating times of the order of hours, is to be expected at typical trapping conditions. However, these simulations did not include collisions with background gas particles. The interplay between such collisions and very energetic micromotion will surely have a significant

heating effect. Hence, even though it is possible to circumvent the regime of large rf heating during the contraction in the cloudlike state and create huge ion plasmas containing 10^5 ions in radio frequency traps, by loading directly into a crystalline or liquidlike state, it remains unclear whether an ordered state in such large plasmas, even once it is established, could be maintained, in the presence of collisions with residual gas atoms.

VII. THE SIGNIFICANCE OF THE FLUORESCENCE DIP

Based on the observations described above, we conclude that the fluorescence dip, in general, is not an indication of a transition into a shell structure, or fully crystalline, regime. Our observations indicate that the fluorescence dip marks the transition into a liquidlike state, and that the formation of shell-structure ordering evolves as a continuous process from that point. This is also in agreement with molecular-dynamics simulations, showing that no real phase transition between the liquid and shell-structure state takes place in finite plasmas [19,21], even when the full time dependence of the confining fields is included [21]. Our observations are, however, not in disagreement with earlier observations, showing that, for small ion plasmas, spatial ordering is present immediately after the dip. Indeed, we observe the same correlation in the case of small prolate plasmas. We do,

however, note that for few-ion plasmas there would be no real difference between a liquidlike and a solidlike state, since it would not be possible to tell short-range and long-range spatial correlations apart.

VIII. CONCLUSION

We have studied the formation process of large ion Coulomb crystals in a linear Paul trap. The experimental results presented in this paper show that for large ion plasmas in radio frequency Paul traps the transition from a disordered cloud state to a liquidlike state is associated with a volume contraction to a finite volume identical with the volume of the fully crystallized ion plasma, a change in aspect ratio towards the aspect ratio expected for a zero-temperature charged liquid and, in most cases (except at very low rf amplitudes), a drop in fluorescence level. This abrupt transition between the cloudlike and liquidlike states was explained as a result of the competition between the laser-cooling force and the rf heating. Once in the liquidlike state, the formation of shell-structure ordering was observed to evolve as a continuous process as the plasma-coupling parameter Γ was further increased. Based on the presented results we conclude that the observation of a fluorescence dip is neither a necessary nor a sufficient condition for identifying a transition into the crystalline state.

-
- [1] F. Diedrich, E. Peik, J. M. Chen, W. Quint, and H. Walther, *Phys. Rev. Lett.* **59**, 2931 (1987).
 - [2] D. J. Wineland, J. C. Bergquist, W. M. Itano, J. J. Bollinger, and C. H. Manney, *Phys. Rev. Lett.* **59**, 2935 (1987).
 - [3] T. W. Hänsch and A. L. Schawlow, *Opt. Commun.* **13**, 68 (1975).
 - [4] D. J. Larson, J. C. Bergquist, J. J. Bollinger, W. M. Itano, and D. J. Wineland, *Phys. Rev. Lett.* **57**, 70 (1986).
 - [5] P. Bøwé, L. Hornekær, C. Brodersen, M. Drewsen, J. S. Hangst, and J. P. Schiffer, *Phys. Rev. Lett.* **82**, 2071 (1999).
 - [6] K. Mølhave and M. Drewsen, *Phys. Rev. A* **62**, 011401(R) (2000).
 - [7] L. Hornekær, N. Kjærgaard, A. M. Thommesen, and M. Drewsen, *Phys. Rev. Lett.* **86**, 1994 (2001).
 - [8] J. I. Cirac and P. Zoller, *Phys. Rev. Lett.* **74**, 4091 (1995).
 - [9] M. D. Lukin, S. F. Yelin, and M. Fleischhauer, *Phys. Rev. Lett.* **84**, 4232 (2000).
 - [10] D. J. Berkeland, J. D. Miller, J. C. Bergquist, W. M. Itano, and D. J. Wineland, *Phys. Rev. Lett.* **80**, 2089 (1998).
 - [11] T. Schätz, U. Schramm, and D. Habs, *Nature (London)* **412**, 717 (2001).
 - [12] G. Birkl, S. Kassner, and H. Walther, *Nature (London)* **357**, 310 (1992).
 - [13] M. Drewsen, C. Brodersen, L. Hornekær, J. P. Schiffer, and J. S. Hangst, *Phys. Rev. Lett.* **81**, 2878 (1998).
 - [14] M. Block, A. Drakoudis, H. Leutner, P. Seibert, and G. Werth, *J. Phys. B* **33**, L375 (2000).
 - [15] S. L. Gilbert, J. J. Bollinger, and D. J. Wineland, *Phys. Rev. Lett.* **60**, 2022 (1988).
 - [16] T. B. Mitchell, J. J. Bollinger, D. H. E. Dubin, X.-P. Huang, W. M. Itano, and R. H. Baughman, *Science* **282**, 1290 (1998).
 - [17] W. M. Itano, J. J. Bollinger, J. N. Tan, B. Jelenkovic, X. P. Huang, and D. J. Wineland, *Science* **279**, 686 (1998).
 - [18] R. Blümel, J. M. Chen, E. Peik, W. Quint, W. Schleich, Y. R. Shen, and H. Walther, *Nature (London)* **334**, 309 (1988).
 - [19] D. H. E. Dubin and T. M. O'Neil, *Phys. Rev. Lett.* **60**, 511 (1988).
 - [20] J. P. Schiffer, in *Proceedings of the Workshop on Crystalline Ion Beams*, edited by R. W. Hasse, I. Hofmann, and D. Liesen (GSI, Wertheim, 1988).
 - [21] J. P. Schiffer, M. Drewsen, J. S. Hangst, and L. Hornekær, *Proc. Natl. Acad. Sci. U.S.A.* **97**, 10697 (2000).
 - [22] J. A. Hoffnagle, R. G. DeVoe, L. Reyna, and R. G. Brewer, *Phys. Rev. Lett.* **61**, 255 (1988).
 - [23] R. G. Brewer, J. Hoffnagle, R. G. DeVoe, L. Reyna, and W. Henshaw, *Nature (London)* **344**, 305 (1990).
 - [24] R. G. Brewer, J. Hoffnagle, and R. G. DeVoe, *Phys. Rev. Lett.* **65**, 2619 (1990).
 - [25] R. Blümel, C. Kappler, W. Quint, and H. Walther, *Phys. Rev. A* **40**, 808 (1989).
 - [26] J. P. Hansen, *Phys. Rev. A* **8**, 3096 (1973).
 - [27] E. L. Pollock and J. P. Hansen, *Phys. Rev. A* **8**, 3110 (1973).
 - [28] W. L. Slattery, G. D. Doolen, and H. E. DeWitt, *Phys. Rev. A* **21**, 2087 (1980).
 - [29] R. W. Hasse and J. P. Schiffer, *Ann. Phys. (Leipzig)* **203**, 419 (1990).
 - [30] M. G. Raizen, J. M. Gilligan, J. C. Bergquist, W. M. Itano, and D. J. Wineland, *J. Mod. Opt.* **39**, 233 (1992).

- [31] By varying the scan rate of the frequency scan away from resonance and extrapolating to an infinitely fast scan rate (i.e., equivalent to turning of the laser light) it was found that the lifetime of an uncooled ion crystal was ~ 10 ms, giving a measure of the equilibration time of the system.
- [32] J. J. Bollinger (private communication).
- [33] L. Turner, Phys. Fluids **30**, 3196 (1987).
- [34] L. R. Brewer, J. D. Prestage, J. J. Bollinger, W. M. Itano, D. J. Larson, and D. J. Wineland, Phys. Rev. A **38**, 859 (1988).
- [35] In this case, it is done by performing a Gaussian blur of the original image, and then subtracting the blurred version of the image from the original, thereby removing slowly varying intensity fluctuations and only keeping the shell-structure details.
- [36] The asymmetry is due to an imperfect compensation for patch potentials on the trap electrodes.
- [37] N. Kjærgaard, L. Hornekær, A. M. Thommesen, Z. Videsen, and M. Drewsen, Appl. Phys. B: Lasers Opt. **71**, 207 (2000).
- [38] The experiment was performed using $^{40}\text{Ca}^+$ ions and the 866-nm repumping laser was chopped and used as a probe.
- [39] Even if the plasma were sufficiently large for bulk structure to appear in the center, such structure would still be surrounded by some 20 shells [17].
- [40] R. Blümel, Phys. Rev. A **51**, 620 (1995).
- [41] J. D. Prestage, A. Williams, L. Maleki, M. J. Djomehri, and E. Harabetian, Phys. Rev. Lett. **66**, 2964 (1991).